Physics of the Earth and Planetary Interiors 230 (2014) 15–27

Contents lists available at ScienceDirect

Physics of the Earth and Planetary Interiors

journal homepage: www.elsevier.com/locate/pepi

Intricate heterogeneous structures of the top 300 km of the Earth's inner core inferred from global array data: I. Regional 1D attenuation and velocity profiles

R. Iritani *, N. Takeuchi, H. Kawakatsu

Earthquake Research Institute, The University of Tokyo, 1-1-1 Yayoi, Bunkyo-ku, Tokyo 113-0032, Japan

ARTICLE INFO

Article history:
Received 28 September 2013
Received in revised form 29 January 2014
Accepted 10 February 2014
Available online 26 February 2014

Keywords:
Inner core
Attenuation
Simulated annealing
Waveform inversion

ABSTRACT

We apply a waveform inversion method based on simulated annealing to complex core phase data observed by globally deployed seismic arrays, and present regional variation of depth profiles of attenuation and velocity for the top half of the inner core. Whereas measured attenuation parameters exhibit consistent trends for data sampling the eastern hemisphere of the inner core, for the western hemisphere, there is a remarkable difference between data sampling the inner core beneath Africa (W1) and beneath north America (W2). Obtained attenuation profiles suggest that intricate heterogeneities appear to be confined in the top 300 km. The profile for the eastern hemisphere has a high attenuation zone in the top 150 km that gradually diminishes with depth. Conversely, for the western hemisphere, the profile for W1 shows constant low attenuation and that for W2 represents a gradual increase from the inner core boundary to a peak at around 200 km depth. Velocity profiles, obtained from differential traveltimes between PKP(DF) and PKP(CD, BC) phases, for the eastern and western hemispheres are respectively about 0.8% faster and 0.6% slower than the reference model at the top of the inner core, and the difference nearly disappears at about 200 km depth. Our result suggests the presence of intricate quasi-hemispherical structures in the top ~200–300 km of the inner core.

1. Introduction

The structure of the inner core has been studied primarily by analyzing seismic core phases (Fig. 1a). PKP(DF) which passes thorough the inner core, and PKP(BC, AB) which passes thorough the outer core or PKP(CD) which is reflected at the inner core boundary (ICB) contain information about the inside and outside of the inner core, respectively. These phases, however, are also affected by the structure of the crust, mantle and strongly heterogeneous D'' layer at the base of the mantle. We usually, therefore, utilize the differential traveltime and amplitude between PKP(DF) and PKP(CD, BC, AB) for structural analyses of the inner core, assuming that the effects from outside of the inner core cancel out each other due to the closeness of ray paths therein.

One of the most peculiar and puzzling seismological properties of the inner core is the presence of the hemispherical heterogeneity in the outermost part of the inner core first reported by Tanaka and Hamaguchi (1997) and later confirmed by many researchers (e.g. Creager, 1999; Niu and Wen, 2001; Cao and Romanowicz, 2004; Yu and Wen, 2006; Tanaka, 2012). It is generally agreed that the eastern (western) hemisphere is characterized by a high (low) velocity and high (low) attenuation shallow layers, which may provide an important clue to constrain the growth processes of the inner core (e.g. Monnereau et al., 2010; Alboussière et al., 2010). There exist, however, considerable discrepancies in the detail of the attenuation and velocity structures among previous studies; for example, by analyzing PKP(DF) and PKP(Cdiff; a diffracted wave along ICB) that globally sampled the inner core, Tanaka (2012) suggested that fast and slow velocity anomalies gradually merge to their average at about 400 km and 250 km depths from ICB, and high attenuation ($Q_P \approx 180$) and low attenuation ($Q_P \approx 300$) layers exist top 250 km and 450 km in the eastern and western hemisphere, respectively. Yu and Wen (2006) reported larger Q_P values than Tanaka (2012) both in the eastern hemisphere and in the western hemisphere. On the other hand, Cao and Romanowicz (2004) obtained similar hemispherical features, but only in the top 85 km of the inner core.

In terms of regional studies, Kaneshima et al. (1994) showed a velocity model beneath the northeastern Pacific (VMOI velocity

* Corresponding author. Present address: Geological Survey of Japan, National Institute of Advanced Industrial Science and Technology, 1-1-1 Higashi, Tsukuba 305-8567, Japan. Tel.: +81 298615420.
E-mail address: r-iritani@aist.go.jp (R. Iritani).

http://dx.doi.org/10.1016/j.pepi.2014.02.002
0031-9201/

model) which is about 0.6% slower than PREM (Dziewonski and Anderson, 1981) at the ICB and linearly merges to the PREM at 300 km depth, and Ohtaki et al. (2012) represented a similar western hemisphere like velocity structure beneath the Antarctica. As to the attenuation structure, the pioneering work of Doornbos (1974) suggested largest attenuation at the top of the inner core and a gradual decrease with depth beneath the northwestern Pacific, while the existence of a high attenuation zone at depths of 200–300 km below the ICB is suggested beneath the northeastern Pacific (Morita, 1991; Kazama et al., 2008; Iritani et al., 2010).

Systematic analyses of globally available waveform data may help to resolve these discrepancies (e.g. Li and Cormier, 2002; Cormier and Li, 2002; Garcia et al., 2006). Particularly, the waveform inversion method based on simulated annealing (SA) adopted by Garcia et al. (2004, 2006) is effective in extracting information about the inner core structure from complicated core phases (Fig. 1). In our earlier study (Iritani et al., 2010), we modified and applied the waveform inversion method for Japanese Hi-net array data, and obtained a continuous 1D attenuation profile beneath the northeastern Pacific that shows a gradual increase of attenuation from ICB with a peak at 200 km depth. While this result is consistent with the previous result for the same region (Morita, 1991; Kazama et al., 2008), it is not so with other studies that show generally low attenuation for the western hemisphere. In this study, we extend the treatment of Iritani et al. (2010) to a large number of globally available broadband seismic array data, and obtain continuous depth profiles of attenuation and velocity structures in various regions of the inner core to systematically investigate the hemispherical heterogeneity. We also note that Iritani (2013) extended the waveform inversion method to discuss the frequency dependence of attenuation and its hemispherical variation to infer the growth process of the inner core.

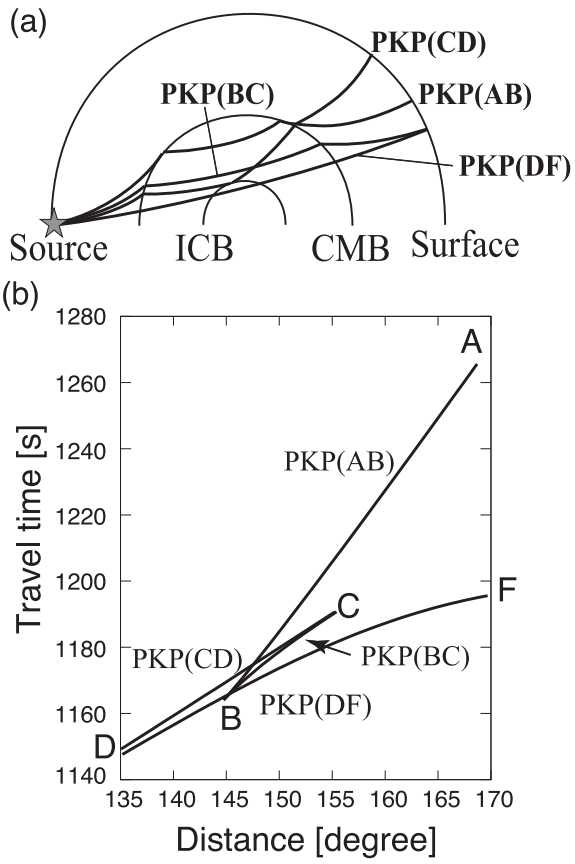

Fig. 1. (a) Illustration of ray paths of core phases. (b) Traveltime curve of core phases for the AK135 model.

2. Data

We analyze the vertical component of broadband velocity seismograms observed by globally expanded seismic arrays that record high-quality core phases. The distribution of stations and events are illustrated in Fig. 2. The waveform data are collected from Japanese F-net, NECESSArray (NorthEast China Extended SeiSmic Array, from Sep. 2009 to Aug. 2011), permanent European stations, USArray and PASSCAL arrays deployed in a number of places in the world for events that occurred from May 1997 to March 2012 with Mw greater than 5.8 (Table 1). Collected core phases sample regions beneath eastern Pacific, North America and Africa in the western hemisphere and almost all areas of the eastern hemisphere of the inner core (Fig. 2). The angle of the ray paths with respect to the earth's rotation axis is greater than 40° (i.e., equatorial paths) for all data sets used in this study, and the effect of anisotropy of the inner core is not significant (Creager, 1999). Each waveform is filtered by a second order zero-phase Butterworth band-pass filter with corner frequencies of 0.35 and 2 Hz,

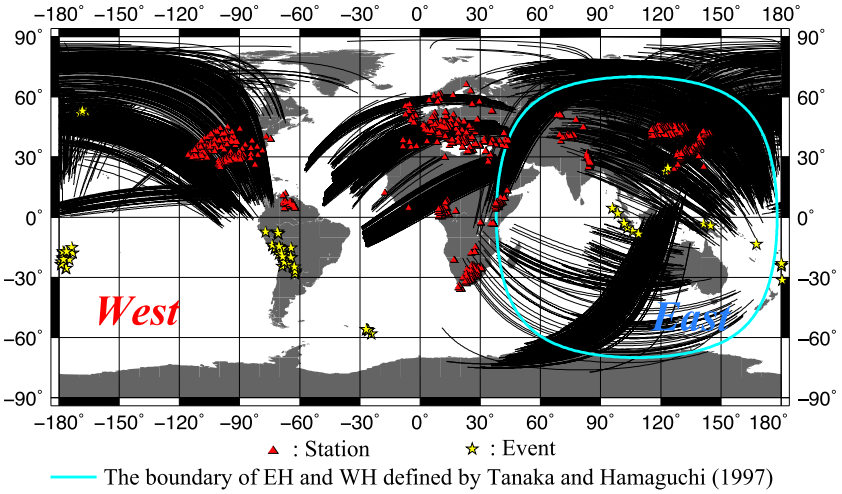

Fig. 2. Distributions of stations (red triangle), events (yellow star) and ray paths (black line) that are used in this study. Ray paths are plotted only for the inner core. The blue line indicates the boundary between the eastern and western hemispheres defined by Tanaka and Hamaguchi (1997). (For interpretation of the references to color in this figure legend, the reader is referred to the web version of this article.)

Table 1
Event list.

Date	Time (GMT)	Lat.	Lon.	Depth (km)	Mw	Array name	Area	Distance coverage	Analysis*
8 May 1997	13:29:26.9	51.8	−170.6	17.0	6.0	PASSCAL	East	143–159°	1
20 July 1997	0:30:26.4	52.3	−167.4	19.0	6.0	PASSCAL	East	143–159°	1
23 Jan. 1998	9:20:10.3	52.1	−168.5	15.0	5.9	PASSCAL	East	145–158°	1
5 Dec. 1998	1:12:49.8	52.0	−169.4	15.0	5.8	PASSCAL	East	147–160°	1
28 Jan. 1999	8:10:8.8	52.9	−169.1	51.1	6.6	PASSCAL	East	143–159°	1
11 March 2001	0:50:45.3	−25.4	−177.6	244.7	5.8	EU	East	135–160°	1
19 May 2001	17:36:32.4	−19.9	−177.2	392.1	5.9	EU	East	137–160°	1
18 June 2001	19:57:1.4	−24.5	−69.6	117.4	5.8	F-net	W2	147–160°	1
29 June 2001	18:35:56.4	−19.7	−66.4	287.2	6.0	F-net	W2	146–160°	1
2 Oct. 2001	0:48:23.2	−16.2	−173.4	108.9	6.1	EU	East	137–159°	1
9 March 2002	12:27:17.1	−56.0	−27.3	127.9	6.0	F-net	East	152–160°	1
16 June 2002	6:55:20.0	−17.6	−178.5	588.1	5.9	EU	East	136–157°	1
27 June 2002	7:16:15.1	−13.4	166.8	194.5	6.0	EU	East	135–144°	2
4 Oct. 2002	19:5:55.2	−20.9	−178.7	650.8	6.3	EU	East	140–154°	1
12 Oct. 2002	20:9:18.5	−8.3	−71.7	539.4	6.9	PASSCAL	W1	150–151°	1
10 Dec. 2002	4:28:1.0	−24.0	179.3	538.8	6.0	EU	East	138–158°	1
4 Jan. 2003	5:15:8.8	−20.7	−177.3	394.7	6.5	EU	East	142–160°	1
27 April 2003	22:57:49.1	−8.2	−71.6	580.2	5.9	PASSCAL	W1	149–150°	1
19 May 2003	10:43:27.3	−18.0	−178.4	578.5	5.9	EU	East	136–160°	1
20 June 2003	6:19:47.4	−7.4	−71.9	556.2	7.0	PASSCAL	W1	149–150°	1
27 July 2003	11:41:31.9	−20.0	−65.2	350.6	6.0	F-net	W2	148–160°	1
27 July 2003	11:41:31.9	−20.0	−65.2	350.6	6.0	PASSCAL	W1	151–157°	1
11 Jan. 2004	9:29:12.7	−20.2	−179.2	682.5	5.9	EU	East	137–160°	1
3 Feb. 2004	23:9:34.4	−3.5	140.6	43.0	5.9	PASSCAL	W2	151–157°	1
17 March 2004	3:21:10.4	−21.2	−65.6	297.0	6.1	F-net	W2	150–160°	1
14 April 2004	1:33:9.5	−17.8	−174.0	144.5	5.9	EU	East	145–158°	1
19 May 2004	7:4:14.2	22.8	121.5	25.0	6.2	PASSCAL	W2	142–150°	1
15 Oct. 2004	4:8:54.9	24.5	122.7	102.1	6.6	PASSCAL	W2	142–148°	1
5 Nov. 2004	5:18:38.3	−4.4	143.9	128.7	5.9	PASSCAL	W2	147–155°	1
12 Nov. 2004	6:36:20.2	−26.9	−63.2	583.1	6.0	PASSCAL	W1	151–152°	1
13 Nov. 2004	7:33:21.4	−26.8	−63.2	582.0	5.8	PASSCAL	W1	151–152°	1
21 Nov. 2004	11:7:19.9	−15.2	−174.6	270.0	5.9	EU	East	140–154°	1
23 Nov. 2004	21:5:0.8	−24.3	179.1	569.4	5.8	EU	East	147–159°	1
21 March 2005	12:23:58.4	−24.9	−63.5	572.3	6.8	PASSCAL	W1	150–152°	1
21 March 2005	12:43:15.0	−24.7	−63.6	572.2	6.4	PASSCAL	W1	150–152°	1
30 March 2005	17:42:0.4	−22.3	−179.6	585.1	6.1	EU	East	137–160°	1
11 April 2005	14:54:10.2	−7.4	−78.0	131.7	6.0	PASSCAL	W1	148–153°	1
16 April 2005	22:41:19.7	−17.8	−69.9	129.6	5.8	PASSCAL	W1	151–154°	1
12 June 2005	19:26:29.4	−56.4	−26.7	97.8	6.0	F-net	East	149–160°	1
26 July 2005	14:11:37.5	−15.4	−73.2	107.6	5.9	F-net	W2	150–160°	1
26 July 2005	14:11:37.5	−15.4	−73.2	107.6	5.9	PASSCAL	W1	152–156°	1
14 Aug. 2005	2:39:42.9	−19.9	−69.4	129.1	5.8	F-net	W2	142–159°	1
14 Aug. 2005	2:39:42.9	−19.9	−69.4	129.1	5.8	PASSCAL	W1	152–155°	1
26 Feb. 2006	3:8:31.8	−23.6	−179.8	553.9	6.4	EU	East	139–159°	1
2 June 2006	7:31:38.0	−20.8	−178.5	584.6	6.0	EU	East	136–160°	1
27 June 2006	2:59:20.0	−19.8	−178.0	596.7	6.3	EU	East	135–155°	1
15 Aug. 2006	23:53:51.2	−21.2	−175.7	162.5	6.1	EU	East	137–158°	1
3 Sept. 2006	22:57:33.4	−23.9	179.0	568.8	5.9	EU	East	138–158°	1
30 Sept. 2006	16:26:59.8	−15.7	−73.3	120.4	5.9	F-net	W2	136–153°	1
3 Oct. 2006	18:3:19.1	−19.0	168.9	166.4	6.3	EU	East	145–155°	1
13 Sept. 2007	16:9:19.6	−3.5	101.2	52.0	6.0	USArray	East	135–144°	2
22 Nov. 2007	23:2:14.5	4.46	95.01	52.1	5.8	USArray	East	135–144°	2
19 Nov. 2007	0:52:16.5	−21.0	−178.6	562.5	6.3	EU	East	141–154°	1
16 Feb. 2008	14:45:15.3	−21.6	−68.8	135.3	6.1	PASSCAL	W1	135–143°	2
14 April 2008	9:45:20.7	−56.0	−27.8	115.2	6.0	F-net	East	147–160°	1
18 April 2008	20:39:12.5	−17.3	−179.0	577.8	6.3	EU	East	145–159°	1
15 May 2008	14:23:33.3	−58.1	−25.2	36.8	5.9	F-net	East	147–160°	1
8 July 2008	9:13:10.0	−16.3	−72.0	125.7	6.2	PASSCAL	W1	137–142°	2
19 July 2008	22:39:56.8	−17.2	−177.1	395.3	6.4	EU	East	135–153°	1
1 Sept. 2008	4:0:40.8	−25.5	−177.3	172.3	6.0	EU	East	141–159°	1
12 Oct. 2008	20:55:44.6	−20.3	−65.2	361.5	6.2	F-net	W2	145–160°	1
17 Dec. 2008	10:56:2.6	−17.8	−178.3	547.8	5.8	EU	East	136–144°	2
12 July 2009	6:12:50.8	−15.3	−70.8	197.1	6.1	F-net	W2	138–155°	1
5 Sept. 2009	3:58:41.6	−15.5	−70.7	209.8	5.8	F-net	W2	138–155°	1
30 Sept. 2009	19:3:22.7	−15.7	−69.7	257.8	5.9	F-net	W2	139–156°	1
30 Sept. 2009	19:3:22.7	−15.7	−69.7	257.8	5.9	NECCESSArray	W2	143–153°	1
16 Oct. 2009	9:52:55.4	−7.1	105.1	45.2	6.1	USArray	East	135–144°	2
22 Nov. 2009	7:48:25.2	−17.7	−178.4	546.4	6.3	EU	East	136–142°	2
22 Nov. 2009	22:47:31.2	−31.5	179.7	437.1	6.2	EU	East	147–160°	1
28 Jan. 2010	8:4:16.9	−23.6	−67.0	204.5	5.9	PASSCAL	W1	136–144°	2
4 March 2010	22:39:29.8	−22.4	−68.7	118.7	6.3	NECCESSArray	W2	149–159°	1
6 May 2010	2:42:53.9	−18.3	−71.3	52.6	6.2	NECCESSArray	W2	145–155°	1
23 May 2010	22:46:55.5	−14.0	−74.5	108.9	6.1	F-net	W2	135–151°	1
23 May 2010	22:46:55.5	−14.0	−74.5	108.9	6.1	NECCESSArray	W2	140–150°	1

(*continued on next page*)

Table 1 (*continued*)

Date	Time (GMT)	Lat.	Lon.	Depth (km)	Mw	Array name	Area	Distance coverage	Analysis*
24 May 2010	16:18:33.6	−8.1	−71.6	591.4	6.4	NECCESSArray	W2	135–144°	2
26 June 2010	9:50:46.3	−8.3	108.0	100.4	5.9	USArray	East	135–152°	1
30 June 2010	4:31:7.2	−23.2	179.3	581.6	6.4	EU	East	137–159°	1
12 July 2010	0:11:26.2	−22.4	−68.6	134.7	6.2	NECCESSArray	W2	150–160°	1
13 Sept. 2010	7:15:50.9	−14.7	−71.1	171.0	5.8	NECCESSArray	W2	142–152°	1
28 Dec. 2010	8:34:22.5	−23.5	−179.7	571.4	6.3	EU	East	139–158°	1
17 Jan. 2011	19:20:59.9	−5.4	102.4	35.4	6.0	USArray	East	135–152°	1
6 March 2011	12:32:2.3	−18.3	−69.7	126.3	6.3	F-net	W2	141–158°	1
6 March 2011	12:32:2.3	−18.3	−69.7	126.3	6.3	NECCESSArray	W2	145–155°	1
6 March 2011	14:32:42.1	−56.4	−26.7	101.2	6.5	F-net	East	149–160°	1
2 April 2011	10:59:42.1	−19.8	−69.5	117.8	5.9	NECCESSArray	W2	146–156°	1
3 April 2011	14:7:14.5	−17.6	−178.4	565.4	6.4	EU	East	137–158°	1
17 April 2011	1:58:51.3	−27.6	−63.1	573.9	5.8	PASSCAL	W1	136–144°	2
8 June 2011	3:6:24.4	−17.4	−69.8	150.4	5.9	PASSCAL	W1	137–142°	2
22 July 2011	6:56:42.8	−20.2	−178.4	605.0	5.9	EU	East	138–160°	1
4 Aug. 2011	0:16:11.2	−3.0	100.8	45.9	5.8	USArray	East	135–151°	1
22 Nov. 2011	18:48:19.2	−15.4	−65.2	553.8	6.6	F-net	W2	141–160°	1
11 Dec. 2011	9:54:59.8	−56.0	−27.8	123.1	6.3	F-net	East	150–160°	1
5 March 2012	7:46:11.9	−28.2	−63.3	565.1	6.1	PASSCAL	W1	140–144°	2

* 1: by waveform inversion as in Section 3.1; 2: by amplitude ratio as in Section 3.2.

and the dominant frequency is about 1 Hz. After waveform inversion analysis, we discard data that appear to suffer from cycle skipping problems and the resultant data set consists of about 4100 traces (out of 6800 traces).

3. Methods of core phase measurements

In the conventional analysis of core phase data, the attenuation parameter and traveltime are measured by comparing PKP(DF) with another core phase to eliminate effects of the crust, mantle, and D'' layer. In this study, depending on the distance range of the record sections we employ different methods: for record sections that involve PKP(BC) phases, we estimate the parameters from the entire record section for each event-array pair via a waveform inversion; on the other hand, for record sections of event-array pairs for which only PKP(DF) and PKP(CD) are observed, we use the amplitude ratio and the differential traveltime for the measurement. Which method is employed for each event-array pair is listed in the last column of Table 1.

3.1. Record section of an event-array pair that involves PKP(BC) phases

To measure attenuation parameters and traveltimes, we employ a non-linear waveform inversion method based on SA that is described in Iritani et al. (2010). SA is a method that can efficiently search for the global minimum in a model space with a large number of parameters (cf. Sen and Stoffa, 1995), and this waveform inversion searches for optimal parameterized model waveforms that well explain observed data according to a SA algorithm. As shown in Fig. 1, core phase data consist of four phases, PKP(DF), PKP(BC), PKP(AB) and PKP(CD), and the distance range that each phase is observed is limited. We thus parameterize model waveforms in two ways depending on the distance range.

For a part of the section for which three core phases (PKP(DF, BC, AB)) are simultaneously observed, each waveform is parameterized as follows:

$$S_i(t) = R_i^{DF} A(t_i^{*DF}) * W(t - \tau_i^{DF}) + R_i^{BC} W(t - \tau_i^{BC}) + R_i^{AB} H * W(t - \tau_i^{AB}) \quad (1)$$

where $S_i(t)$ is a time series of the model waveform of station i; $W(t)$ is a reference waveform which indicates a representative incident wave to the array; R_i^{DF}, R_i^{BC}, R_i^{AB} are amplitude parameters that combined the effects of the source radiation, geometrical spreading and transmissions at boundaries in the earth; τ_i^{DF}, τ_i^{BC}, τ_i^{AB} are traveltimes of respected phases; $A(t_i^{*DF})$ is the differential attenuation operator between PKP(DF) and reference waveform assuming a constant Q (e.g. Aki and Richards, 1980), and it is defined as,

$$A(t^*) = \int_{-\infty}^{\infty} \exp\left(-\frac{\omega t^*}{2} + i\frac{\omega t^*}{\pi}\log\frac{\omega}{\omega_0}\right) e^{i\omega t} d\omega \quad (\omega_0 = 2\pi) \quad (2)$$

where ω, ω_0 are the angular frequency and the reference angular frequency of PKP(DF); and H represents the Hilbert transform operator and asterisk denotes convolution. As in the previous studies, we do not include PKP(CD) in the modeling because of its small amplitude.

For the rest of the record section for which the three core phases are not simultaneously observed, we model only PKP(DF) waveforms as

$$S_i(t) = R_i^{DF} A(t_i^{*DF}) * W(t - \tau_i^{DF}) \quad (3)$$

and we use $W(t)$ determined from the triplicated distance range.

The optimization process in our waveform inversion is based on that of Iritani et al. (2010). We first estimate unknown parameters in Eq. (1), $W(t)$, $R_i^{DF,BC,AB}$, $\tau_i^{DF,BC,AB}$, t_i^*, by using triplicated data. As for initial values, we set $W(t) = 0.0$, $R_i^{DF,BC,AB} = 1.0$, and $t_i^* = 0.001$; for τ_i^{DF}, τ_i^{BC} and τ_i^{AB}, we use theoretical traveltimes of respective phases for the reference velocity model, AK135 (Kennett et al., 1995). We then perturb these parameters iteratively and calculate L1 norm misfit function,

$$E = \sum_i \int |D_i(t) - S_i(t)| dt \quad (4)$$

where $D_i(t)$ is an observed waveform at station i. In each step, the reference waveform and amplitude corrections are perturbed randomly by 1% of the maximum amplitude of the observed record section within a given range; only when the misfit function, E, decreases, new parameters are accepted. For traveltimes $\tau_i^{DF,BC,AB}$ and attenuation parameter t_i^{*DF}, new parameters are given by random values within predetermined ranges, and the acceptance is evaluated by following Boltzmann criterion that depends on E and the number of iterations (e.g. Chevrot, 2002; Garcia et al., 2004). Next we apply the same approach to the rest of core phase data by using Eq. (3) with fixing $W(t)$, and estimate R_i^{DF}, τ_i^{DF}, and t_i^*. (Iritani et al., 2010 describes more detail of the SA algorithm.) We execute these processes 20 times for each event-array data set with

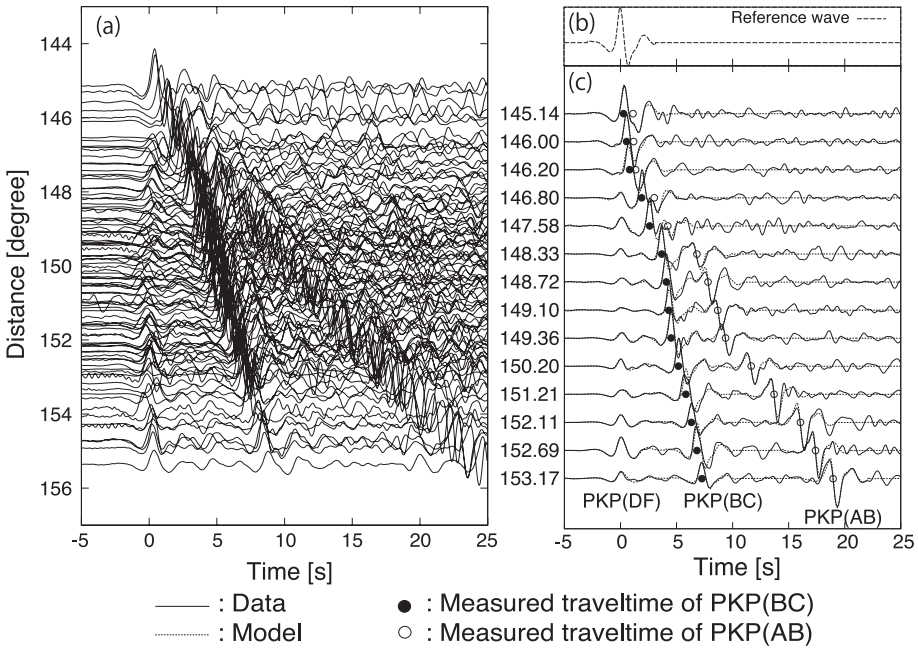

Fig. 3. Example of the waveform inversion. (a) A record section observed by NECESSArray for an event in South America (4 March 2010). Waveforms are aligned by theoretical traveltimes of PKP(DF). (b) The reference waveform obtained by the waveform inversion. (c) Comparison between data (solid line) and model waveforms (dotted line). Both waveforms are aligned by the measured traveltime of PKP(DF). Black and open circles represent measured traveltimes of PKP(BC) and PKP(AB), respectively.

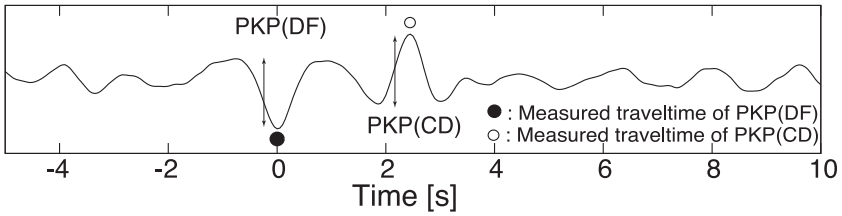

Fig. 4. Filtered seismogram of a South American event (23 May 2010) observed by NECESSArray at an epicentral distance of 139°. Black and open circles respectively denote measured traveltimes of PKP(DF) and PKP(CD), and arrows indicate measured amplitude.

different random seeds, and the average and standard deviation of estimated parameters are defined as the measured optimal parameters and their errors.

An example of the waveform inversion analysis is presented in Fig. 3. Although three core phases overlap each other for a distance range of 145–147° where conventional approaches have difficulties, observed data are well fit by the optimal waveforms, and estimated traveltimes appear robust (Fig. 3c).

3.2. Record section of an event-array pair without PKP(BC)

For an event-array pair for which PKP(BC) used as a reference phase in the waveform inversion is absent and only PKP(DF) and PKP(CD) are observed in the entire record section, the waveform inversion method cannot be simply applied because of the difficulty of modeling PKP(CD) that is in the retrograde branch (e.g. Aki and Richards, 1980) as a reference phase. Therefore, we employ a conventional approach and use the amplitude and traveltime. We measure the peak to peak distance as the amplitude and the time of the maximum amplitude as the traveltime for each phase under the assumption that the phase difference between PKP(DF) and PKP(CD) is 180° (Fig. 4). The attenuation parameter of the inner core is then obtained from the amplitude ratio PKP(DF) to PKP(CD). Assuming the ray theory, the amplitude of core phase is affected by the radiation pattern, geometrical spreading, attenuation in the mantle, and the transmission/reflection at discontinuities in the earth. By correcting these effects other than the attenuation of the inner core, t^*_{IC} can be obtained as

$$t^*_{IC} = -\frac{1}{\pi f}\ln\frac{A_{DF}}{A_{CD}} \tag{5}$$

where A_{DF} and A_{CD} are the corrected amplitudes of PKP(DF) and PKP(CD), respectively. In calculation of the attenuation parameter, we assume 1 Hz as the reference frequency (f in Eq. (5)). The adequacy of this approach is tested by using full-waveform DSM synthetics (Kawai et al., 2006) for AK135 up to a distance $\sim$ 143.4°: the accuracy of measurements is about 0.05 s for t^*_{IC} and 0.1 s for the differential time for noise free synthetics. We also confirm in the later section (4.1.1) that there is no systematic bias between the measurements of t^* by the waveform inversion and the hand pick measurements employed here. Although the CMB scattered precursors to PKP may potentially contaminate PKP(DF) at distances greater than around 140°, such bias is also not confirmed.

4. Results

4.1. Attenuation

4.1.1. Attenuation parameters, t^*

In the waveform inversion employed in this study (except for the case in Section 3.2), attenuation parameters are measured by broadening of PKP(DF) relative to the reference waveform $W(t)$,

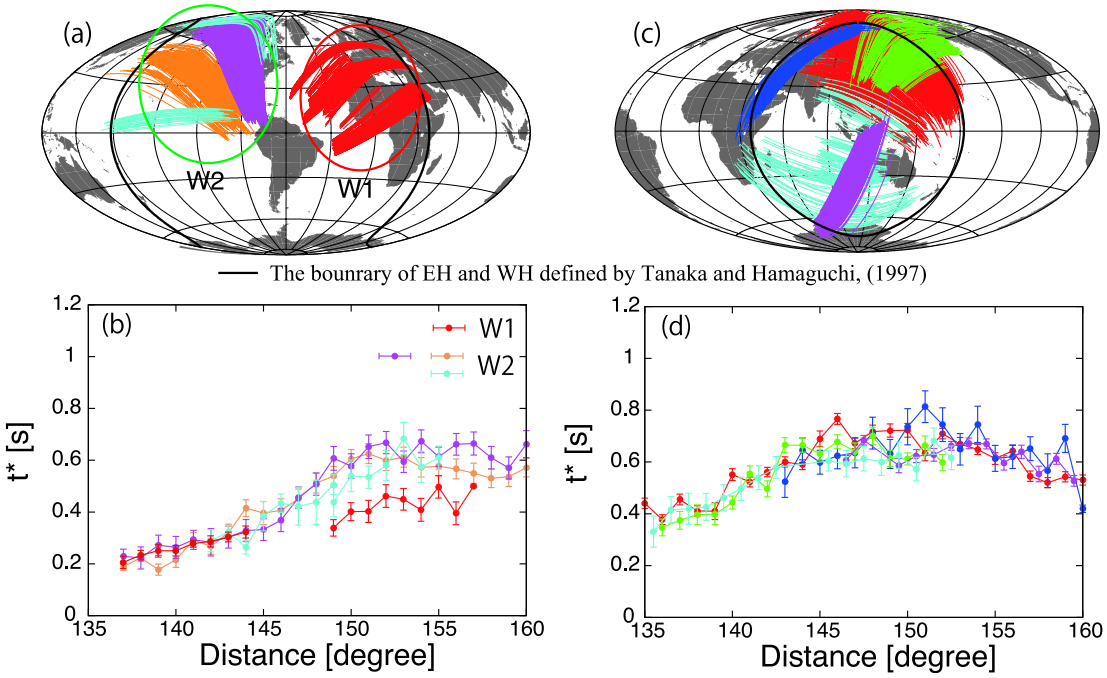

Fig. 5. (a) Ray paths of PKP(DF) that sample the western hemisphere. The black solid line indicates the boundary between the hemispheres defined by Tanaka and Hamaguchi (1997). Data in the red circle show relatively small attenuation parameter in the distance range between 148–157° (W1), and those in the green circle show gradual increase over the distance of 147° (W2). (b) Measured attenuation parameters averaged for a distance bin of 1° are plotted. (c and d) Ray paths and measured attenuation parameters for data that sample the eastern hemisphere. The error bar in (b) and (c) denotes a standard error and different colors in (b) and (d) correspond to the paths in the same color in (a) and (c). (For interpretation of the references to color in this figure legend, the reader is referred to the web version of this article.)

which is unique for each event-array pair and is estimated from the entire core phases within the distance range where three core phases are observed. Assuming the outer core attenuation is negligible, therefore, the difference between ray paths in the mantle for PKP(DF) and PKP(BC) affect the measurement of the attenuation parameter. We evaluate and correct for this effect as follows. First, we calculate the theoretical t^* value of PKP(BC) in the mantle for a given attenuation model (PREM), and consider the average as the t^* value of the reference waveform. Then, we correct the residual between the theoretical t^* of PKP(DF) in the mantle and the t^* of the reference waveform for each data. The overall corrections values of this effect are around 0.035.

After the correction for the effects of the mantle, attenuation parameters are averaged over 1° bins for each event-array pair and plotted as a function of epicenter distance for a source depth of 0 km. Measured attenuation parameters show a clear hemispherical variation for a distance range 135–147°: t^* in the western hemisphere vary from 0.2 to 0.4 and t^* in the eastern hemisphere show larger values than the western hemisphere and vary from 0.4 to 0.6. In the distance range over 148°, t^* in the western hemisphere shows two different trends: while the data that sample beneath the western Atlantic and Africa (red circle in Fig. 5a) show slight increase of t^* from 0.4 at 148° to 0.45 at 157°, the data that sample beneath the northeastern Pacific and north America (green circle in Fig. 5a) show a relatively large increase of t^* from 0.4 at 147° to 0.6 at 151° and become nearly constant value of 0.6 in the farther distance range (Fig. 5b). On the other hand, t^* for the eastern hemisphere have a nearly constant value of 0.6 at a distance range 147–155° that appear to decrease beyond. The general trend of the eastern hemisphere data is consistent for all event-array data for all distance ranges (Fig. 5d), indicating that a similar structure extends in a wide region of the eastern hemisphere from shallow to deep.

The depth (from the ICB) of the turning point of PKP(DF) for a distance of 148° is about 150 km, and it suggests the existence of lateral heterogeneity of attenuation structure below this depth in the western hemisphere. We, thus, separate the data for the western hemisphere into two groups, which we refer to as W1 for the data that sample beneath the western Atlantic and Africa and W2 for the data that sample beneath the northeastern Pacific and north America (Fig. 5a). The result for W2 is consistent with the result of Kazama et al. (2008), who estimated the structure of the top half of the inner core beneath the northeastern Pacific by amplitude ratio between PKP(DF) and PKP(BC, AB). Fig. 6 illustrates comparisons of PKP(DF) waveforms stacked for 1° bins around 137°, 143° and 150° for each sampling region. Waveforms for W2 show a larger broadening with distance compared to waveforms for W1 and the eastern hemisphere confirming the presence of attenuative region in W2.

Similar features can be confirmed from the measurement of the amplitude. As we mentioned in the first paragraph of this section, attenuation parameters of the inner core are measured by broadening of PKP(DF) with respect to the reference waveform, and it differs from more conventional differential methods those directly compare core phases within each seismogram (e.g. Doornbos, 1974; Kazama et al., 2008). Thus, it is possible that properties unique to individual stations are reflected in the attenuation measurements. To check the robustness of the measurements by the waveform inversion (data analyzed as in Section 3.1), we compare obtained attenuation parameters with values measured by amplitude ratios of PKP(DF) to PKP(BC, CD). We measure the peak-to-peak amplitude of PKP(DF) and PKP(BC, CD) manually for each data ($R^{DF,BC}$ obtained by the waveform inversion, if properly corrected for the q-filter effect, give similar results). The mantle-path-corrected amplitude ratios show a consistent trend with t^*, indicating significant differences between the western and eastern hemispheres for a distance range of 135–143° from the amplitude ratio between PKP(DF) and PKP(CD) (Fig. 7a) and between W1 and W2 for a distance range over 148° from the amplitude ratio between PKP(DF) and PKP(BC) (Fig. 7b). It should be noted here that the

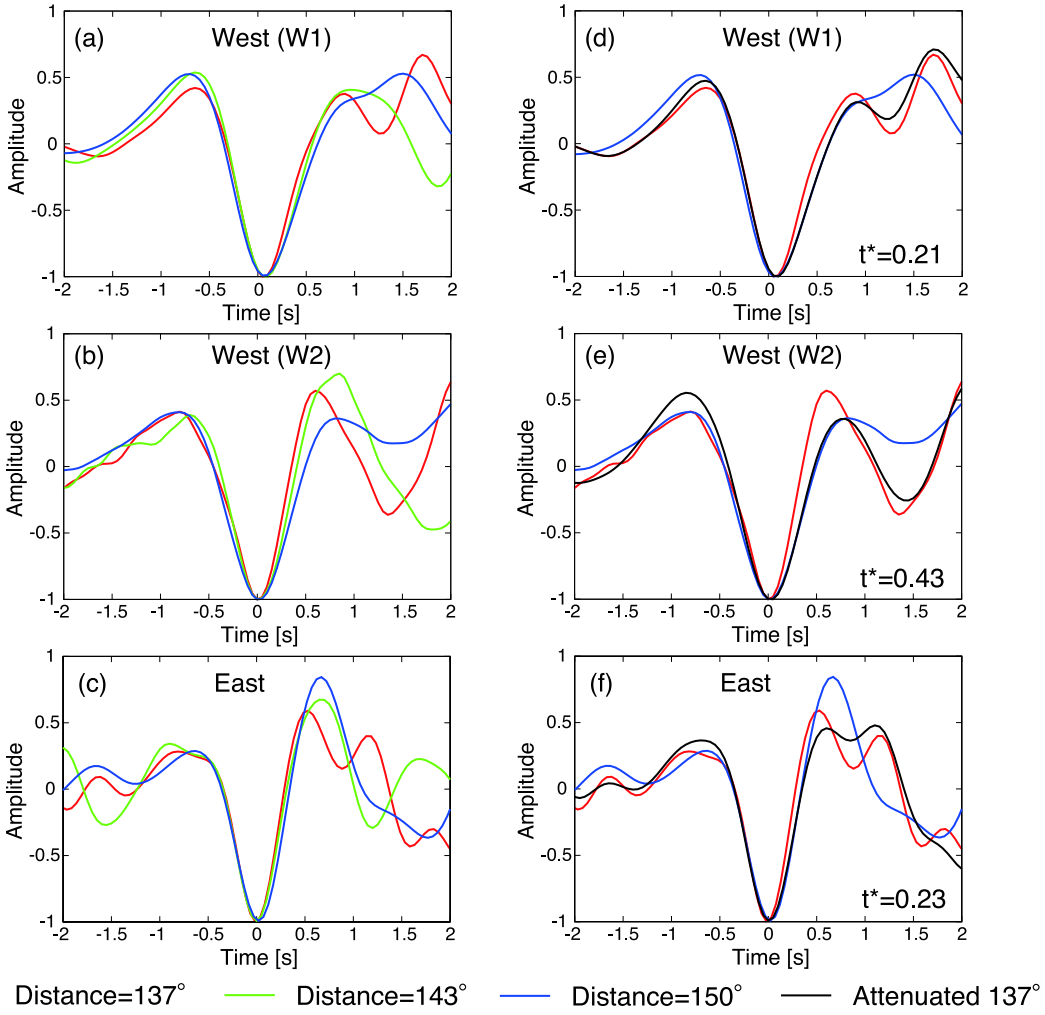

Fig. 6. (a–c) Comparison of stacked PKP(DF) phases for distance bins of 1° around 137° (red), 143° (green) and 150° (blue) for (a) W1 (event 19 July 2008 in Table 1), (b) W2 (8 June 2011) and (c) the eastern hemisphere (26 July 2005). (d–f) Similar to (a–c), but the observed waveform at 150° (blue) is compared with the waveform of 137° convolved with the attenuation filter with a differential value indicated at the right-bottom corner of each box (black). Waveforms are normalized by the maximum amplitudes. (For interpretation of the references to color in this figure legend, the reader is referred to the web version of this article.)

amplitude measurements employed in Section 3.2 are included for the distance range of 135–143° (Fig. 7a). Those correspond to the entire measurements for W1 (red points in Fig. 7a), ~5% measurements for W2 (green), and ~15% for East (blue).

Fig. 8 shows a comparison of t^* measured by the waveform inversion and by the amplitude ratio for the same event-array datasets analyzed as in Section 3.1. As these measurements are independent to each other, correlation slopes nearly one (correlation coefficients are 0.76 for the western hemisphere and 0.72 for the eastern hemisphere) indicate that there is no systematic bias introduced in measurements obtained by the waveform inversion, although large uncertainty remains for individual measurements (shown as data points in the figure) (cf. Iritani et al., 2010).

4.1.2. Attenuation profile

Using the observed attenuation parameters, we invert for attenuation profiles of the top half of the inner core via the conventional least-squares method. For the inversion, we use individual t^* measurements corrected for the effects of the mantle attenuation. t^* for a layered earth may be written by using quality factor Q as follows,

$$t_i^* = \sum_{j=1}^{n} \frac{T_{ij}}{Q_j} \tag{6}$$

where t_i^* is the attenuation parameter for the ith ray path, T_{ij} is the traveltime for the ith ray path in the jth layer of the inner core, Q_j is the quality factor of the jth layer of the inner core, and n is the total number of layers. Since attenuation parameters show the consistent trend in the eastern hemisphere and the significant difference between W1 and W2 in the western hemisphere, we solve for one representative attenuation model for the eastern hemisphere by using all data that sample the eastern hemisphere, and two models for the western hemisphere using the data of W1 and W2 separately. We define 10 layers with a thickness of 50 km in the top 500 km of the inner core for the model of the eastern hemisphere and W2 of the western hemisphere; for the model of W1 of the western hemisphere, because of the limited distant coverage (137–144°, 149–157°), we define 4 layers with a thickness of 100 km in the top 400 km of the inner core.

The obtained attenuation profiles are shown in Fig. 9a. The attenuation model for the eastern hemisphere has a high attenuation ($Q^{-1} = 0.006$) zone near the ICB, and the attenuation gradually decreases with depth (blue line in Fig. 9a). For the western hemisphere, the model for W1 shows nearly a constant low attenuation ($Q^{-1} \approx 0.003$) and the model for W2 shows a gradual increase with depth with a peak at around 200 km. Below a depth of 300 km of the inner core, three attenuation models show similarly small attenuation ($Q^{-1} \approx 0.002$); this may indicate that the inner core

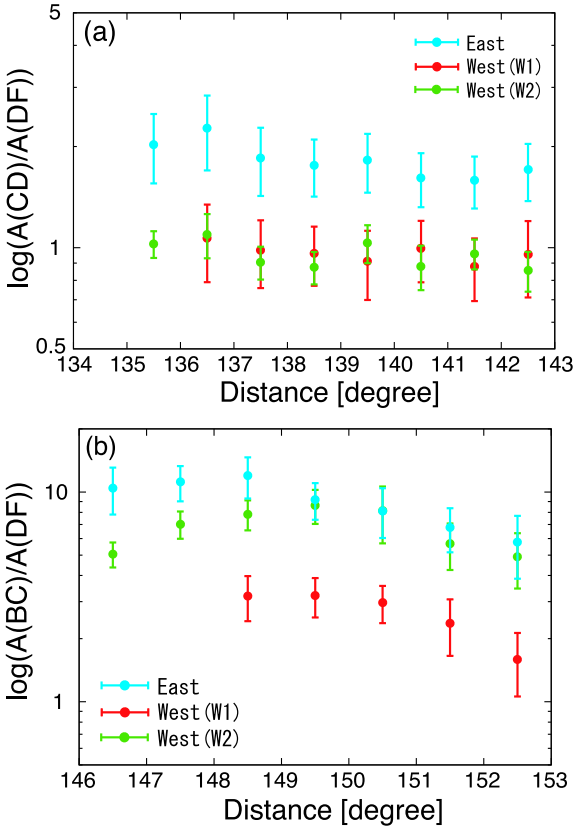

Fig. 7. Comparison of measured amplitude ratios: (a) PKP(CD)/PKP(DF) and (b) PKP(BC)/PKP(DF) for W1 (red), W2 (green) and the eastern hemisphere (blue). Averaged values for each hemisphere for a distance bin of 1° and their standard errors are plotted. (For interpretation of the references to color in this figure legend, the reader is referred to the web version of this article.)

is similar in all regions below 300 km, and the hemispherical heterogeneity is restricted in the top 300 km of the inner core. The theoretical values calculated using obtained models well explain the observed data (Fig. 9b and c).

4.2. P-wave velocity

4.2.1. Differential traveltimes

The depth variation of the P-wave velocity structure of the top half of the inner core is estimated from differential traveltimes between PKP(DF) and PKP(CD) or PKP(BC). For the actual inversion of the velocity structure, we use the residual between the observed and theoretical values of the differential traveltime of PKP(BC, CD) and PKP(DF), Δt_i:

$$\Delta t_i = \left(\tau_i^{BC,CD} - \tau_i^{DF}\right) - \left(t_i^{BC,CD} - t_i^{DF}\right) \quad (7)$$

where $\tau_i^{BC,CD}$ and τ_i^{DF} are measured traveltimes and $t_i^{BC,CD}$ and t_i^{DF} are theoretical traveltimes calculated for AK135 reference model of PKP(BC, CD) and PKP(DF) at a station i, respectively. A positive residual denotes faster arrival of PKP(DF) (slower arrival of PKP(BC)) and a negative residual denotes slower arrival of PKP(DF) (faster arrival of PKP(BC)) with respect to the reference model. Fig. 10 presents measured traveltime residuals as a function of distance, averaged for each event-array pair with a distance bin of 1°. For the data that sample the western hemisphere, negative traveltime anomalies are observed throughout the distance range with small fluctuations (Fig. 10a), even though measured attenuation parameters show the difference between W1 and W2. On the other hand, for the data that sample the eastern hemisphere, all data show

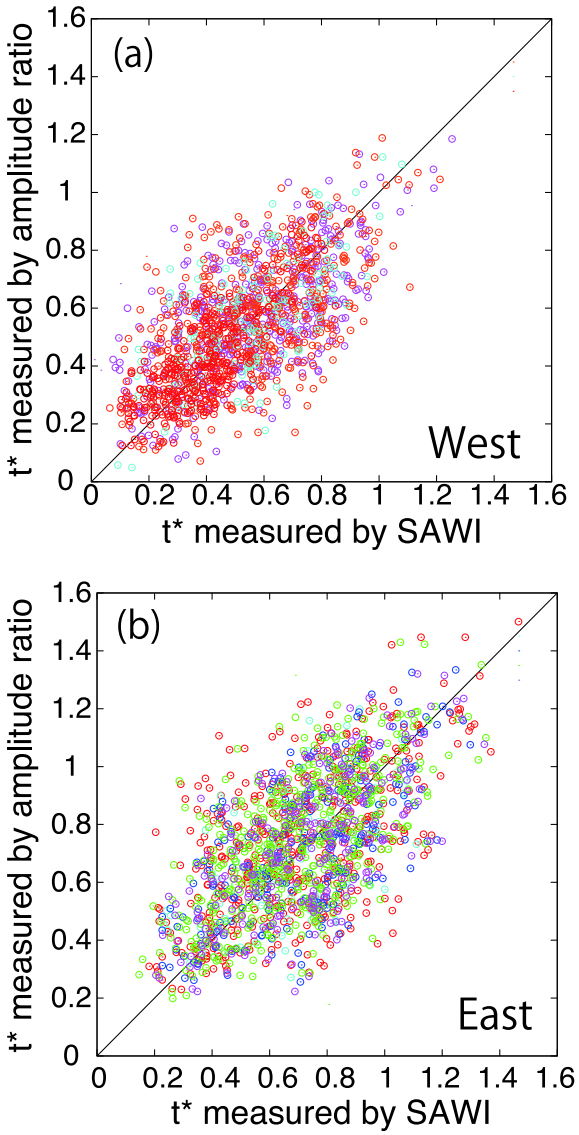

Fig. 8. t^*s measured by the simulated annealing waveform inversion (SAWI) are compared with those measured by the amplitude ratio of PKP(DF) to PKP(BC, CD): (a) for the western hemisphere and (b) for the eastern hemisphere. Different colors correspond to the different arrays shown in Fig. 5a and c. (For interpretation of the references to color in this figure legend, the reader is referred to the web version of this article.)

positive traveltime anomalies; while a consistent trend is observed for the most of event-array pairs, relatively small positive anomalies are observed for the USArray data for events in Indonesia (Fig. 10b). As ray paths of PKP(DF) for Indonesia-USArray pairs go across the boundary between two hemispheres by sampling both hemispheres considerably (Fig. 5c), we interpret that the small traveltime residuals are due to the result of canceling effect of the hemispherical anomalies and omit this data set from further modeling for the depth profile.

4.2.2. Velocity model

Based on the ray theory, a traveltime anomaly can be written as,

$$\Delta t_i = \int_i \frac{\Delta u}{u} u \, dl \quad (8)$$

where Δt_i is the traveltime residual for the ith ray path, u is the slowness of the inner core, $\Delta u/u$ is the fractional perturbation of the slowness, and dl represents the length of an infinitesimal

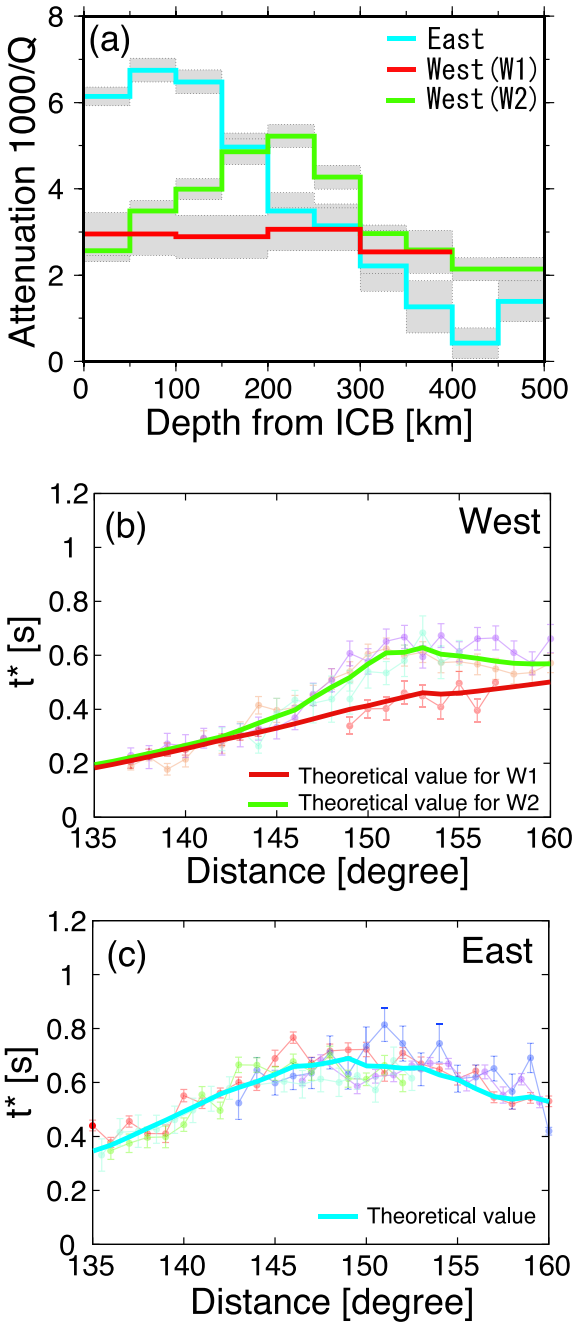

Fig. 9. (a) Attenuation profiles for W1 (red), W2 (green) and the eastern hemisphere (blue). The model errors are shown by shadows. (b and c) A comparison between theoretical values calculated using obtained attenuation models and averaged t^* by the distance bin of the 1° for the western hemisphere (b) and the eastern hemisphere (c). (For interpretation of the references to color in this figure legend, the reader is referred to the web version of this article.)

segment along the ray path. We parameterize the perturbation of slowness by a summation of cubic b-splines,

$$\frac{\Delta u}{u}(r) = \sum_{k=1}^{m} a_k B_k(r) \tag{9}$$

where $B_k(r)$ is the b-spline basis function, a_k is the coefficient for each b-spline basis function with a knot interval of 100 km, m is the total number of b-spline functions, and r is the radius. The estimated profile $V_{\mathrm{New}}(r)$ is give by the reference velocity, $V_{\mathrm{Ref}}(r)$ as

$$V_{\mathrm{New}}(r) = V_{\mathrm{Ref}}(r)\left(1 - \frac{\Delta u}{u}(r)\right). \tag{10}$$

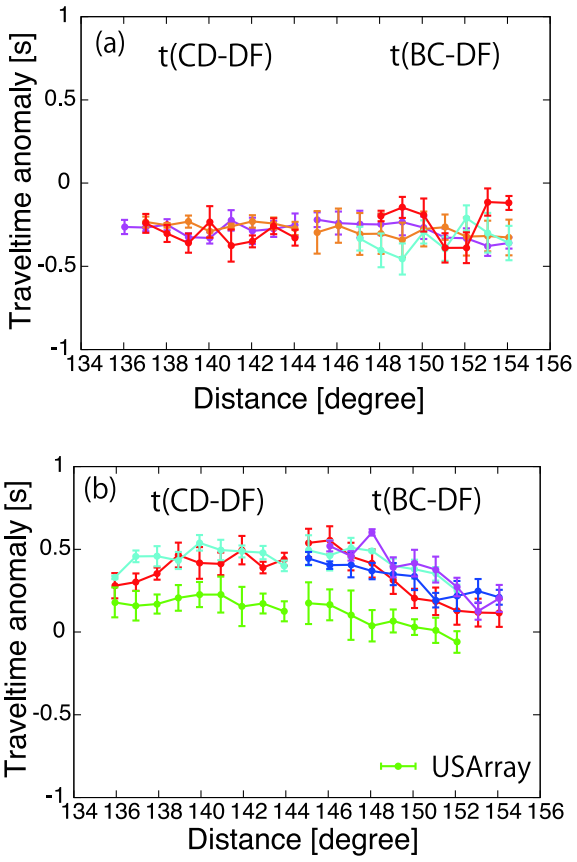

Fig. 10. Measured differential traveltime residuals referenced to AK135. Averaged values for each array for a distance bin of 1° are plotted; the distance range of 136–144° and 145–155° correspond the differential traveltime of PKP(DF)–PKP(CD) and PKP(DF)–PKP(BC), respectively. The error bar denotes the standard error and colors in (a) and (b) correspond to ray paths in Fig. 5a and c. (For interpretation of the references to color in this figure legend, the reader is referred to the web version of this article.)

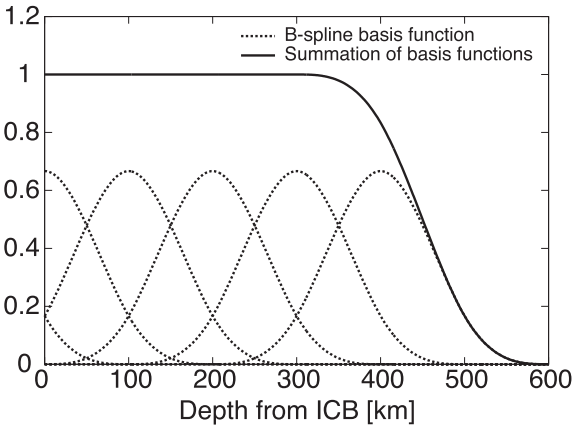

Fig. 11. B-spline basis functions used in the analysis (dotted lines) and their summation (solid line).

Since the arrival of the PKP(BC) is limited up to a distance of 155°, traveltime residuals are available to this distance range and the resolvable depth range is down to ~350 km from the ICB. Thus, we use 6 b-spline basis functions and estimate the velocity structure of the top 350 km of the inner core (Fig. 11). In the actual inversion, individual values of Δt are used and 6 coefficients, a_k, are obtained by the conventional least-squares method; the error bar of the estimated velocity model, $E(V_{\mathrm{New}})$, is calculated by

$$E(V_{\mathrm{New}}) = V_{\mathrm{Ref}} E\left(\frac{\Delta u}{u}(r)\right) = V_{\mathrm{Ref}} \sum_{k=1}^{m} E(a_k) B_k(r) \tag{11}$$

where $E(\Delta u/u)$ is the error of the slowness perturbation and $E(a_k)$ is the error of the b-spline coefficient calculated from the diagonal component of the posterior-covariance matrix. Since the measured traveltime residuals show consistent trends in each hemisphere except for the USArray data (for Indonesian events), we construct a representative velocity profile for each hemisphere.

4.3. Trade off between the base of the outer core and the inner core

The velocity structure of the inner core cannot be uniquely determined only by the traveltime residuals because there is a trade-off between the velocity structure of the inner core and the base of the outer core. The positive (negative) residual can be explained not only by a faster (slower) anomaly in the inner core, but also by a slower (faster) anomaly at the base of the outer core. Tanaka (2012) measured the amplitude ratio and differential traveltime between PKP(DF) and PKP(Cdiff) from global core phase data sets, and suggested that AK135 which has a small velocity gradient at the base of the outer core is more reasonable than PREM which has a relatively large velocity gradient. This view is consistent with other previous studies (Souriau and Roudil, 1995; Cormier, 2009). On the other hand, in a regional study, Kaneshima et al. (1994) studied the velocity structure beneath northeastern Pacific, and suggested a larger velocity gradient in the 300 km range above ICB and about 0.35% faster velocity at the base of the outer core compared to AK135 (VMOI model).

To investigate the degree of the tradeoff between the outer core and inner core velocity structure, we employ three velocity models for the base of the outer core: AK135, VMOI and the Middle model which has middle values between AK135 and VMOI in 100 km above the ICB, while the same as AK135 for the rest. For each of the employed outer-core velocity models, we invert for an inner core velocity profile using the measured traveltime residuals

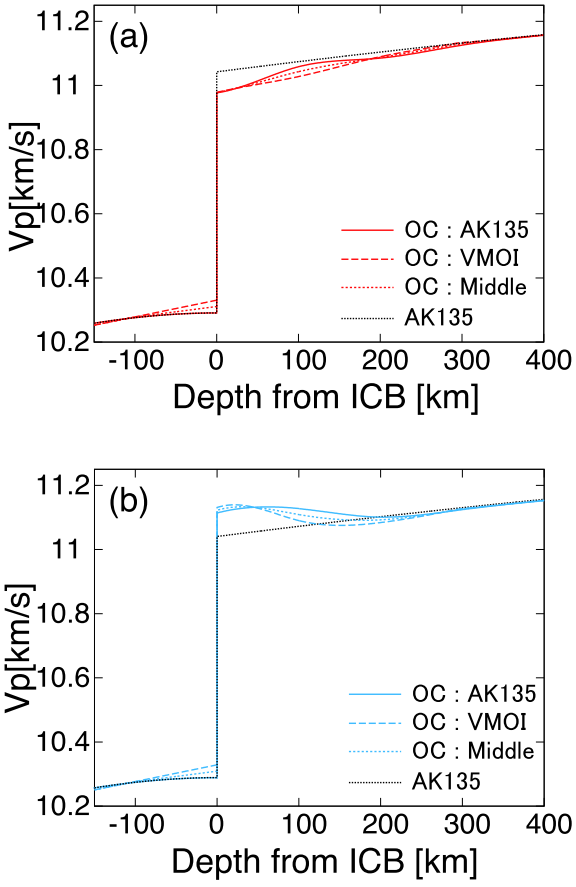

Fig. 12. Velocity models inverted for the same traveltime data by using three velocity models of the outer core, AK135 (solid line), VMOI (dashed line), the model that have middle value of AK135 and VMOI at the ICB (dotted line) for (a) the western hemisphere and (b) the eastern hemisphere. AK135 model is also plotted as a reference by black dots.

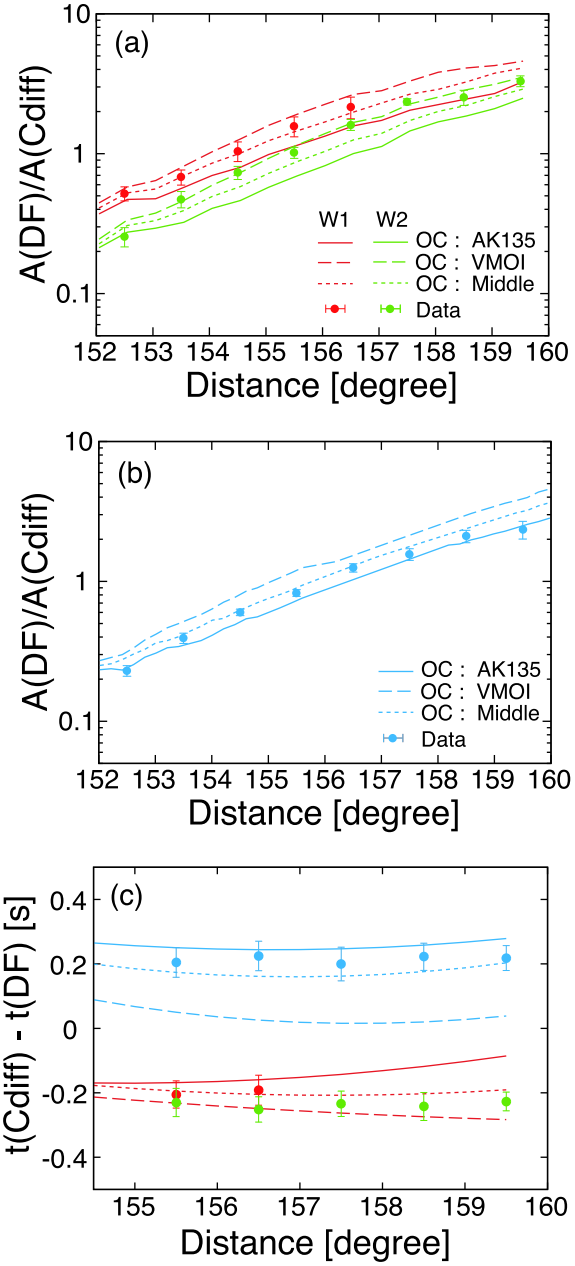

Fig. 13. (a and b) Comparisons of measured amplitude ratio of PKP(DF)/PKP(Cdiff) (1° bin average) with prediction from models in Fig. 12 for the western hemisphere (a) and the eastern hemisphere (b). Solid, dashed and dotted lines denote prediction based on corresponding velocity models in Fig. 12 and error bars are standard errors. (c) Comparisons of measured differential traveltime residuals between PKP(DF) and PKP(Cdiff) relative to AK135. Red and blue lines represent theoretical values for the western and eastern hemisphere respectively, and line types are same as (a and b). Measured data for W1 (red), W2 (green) and the eastern hemisphere (blue) are averaged by the distance bin of the 1°. (For interpretation of the references to color in this figure legend, the reader is referred to the web version of this article.)

(Fig. 10) for two hemispheres (Fig. 12). Robustness of models is examined by comparing amplitude ratios and differential traveltimes between PKP(DF) to PKP(Cdiff). Here, we measure the peaks of these phases by hand, and the amplitude and traveltime are defined by the peak to peak and the time of the maximum peak, respectively. Theoretical amplitude ratios and differential traveltimes are estimated from DSM synthetics (Kawai et al., 2006) calculated with the attenuation models estimated in the previous section (Fig. 9a). The results shown in Fig. 13 indicates that the velocity models obtained by assuming the Middle outer core model (dotted lines) reasonably explain both of observed amplitude ratios and differential traveltimes for both hemispheres except for W2. As for the W2 region, the model with the VMOI outer core fits data slightly better, which is consistent with Kaneshima et al. (1994) as their studied area corresponds to W2, but the difference may not be significant as shown later in the waveform data.

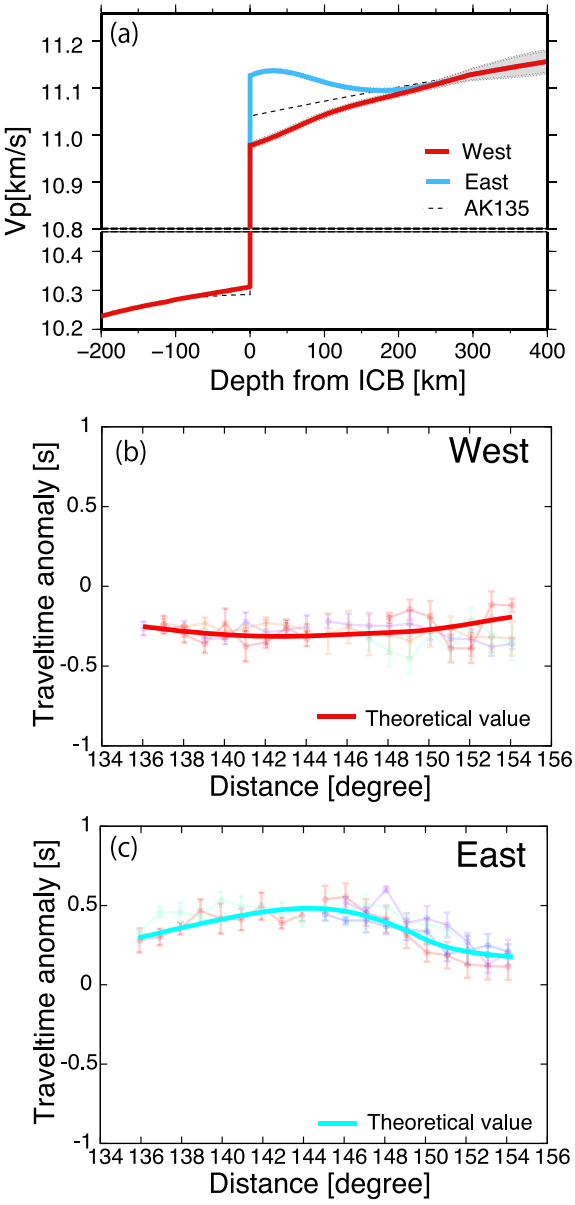

Fig. 14. (a) Velocity profiles for the western hemisphere (red) and the eastern hemisphere (blue) inverted by using the Middle outer core velocity model. The model errors are shown by gray shadow. AK135 model is also plotted by broken line. (b and c) Comparisons between theoretical values calculated by using the best velocity models and measured values of the differential traveltime for the western hemisphere (b) and the eastern hemisphere (c). (For interpretation of the references to color in this figure legend, the reader is referred to the web version of this article.)

Table 2
B-spline coefficients, a_k, for the best velocity profiles.

	B-spline coefficients ($\times 10^{-3}$)					
	a_1	a_2	a_3	a_4	a_5	a_6
WEST	−4.536	−6.949	−1.831	−1.591	0.1634	0.05501
EAST	−4.439	12.07	2.872	−1.526	0.1654	0.05477

Based on the above results, we adopt the Middle model as a common velocity model for the base of the outer core, and obtained velocity profiles for both hemispheres as the best models are shown in Fig. 14a (corresponding b-spline coefficients, a_k, are presented in Table 2). The fit of the theoretical differential traveltime residuals between PKP(DF) and PKP(BC, CD) calculated for the obtained velocity profiles to data are shown in Fig. 14b and c. The inner core velocity profile for the western hemisphere shows 0.6% slower velocity anomaly at the ICB that gradually merges to AK135 at about 200 km depth. On the other hand, the eastern hemisphere shows 0.8% faster anomaly at the ICB that merges to AK135 at about 200 km depth. These features of heterogeneities are generally consistent with the results of Tanaka (2012), but the depth that heterogeneities disappear is shallower than the depth suggested by Tanaka (2012). It should be noted that, regardless of the choice of the outer core model, the feature that the eastern hemisphere show the faster velocity than the western hemisphere dose not change and the absence of heterogeneities below ~200 km depth of the inner core neither (Fig. 12).

5. Discussion and conclusion

In this study, we obtain depth profiles of the attenuation and velocity structures in various regions of the inner core for the equatorial ray paths, and identify intricate differences between the eastern and western hemispheres. The hemispherical heterogeneity disappears below a depth of ~300 km where attenuation is generally weak ($Q^{-1} \sim 0.002$). The eastern hemisphere exhibits higher attenuation and faster velocity than the western hemisphere above this depth. Moreover, we observed a lateral heterogeneity of attenuation inside of the western hemisphere that can be confirmed in observed waveforms. Fig. 15 shows comparisons between observed and full-wave synthetic waveforms. Fig. 15a is for data observed by the Tibetan array (26 July 2005) which sample in W1, and Fig. 15b is for data observed by NECESSArray (4 March 2010) which sample in W2. Synthetics are calculated by the DSM method for attenuation models for W1 and W2 with the velocity model for the western hemisphere (red line in Fig. 12). We use the Global CMT catalog for source parameters. For both regions, synthetic waveforms calculated for the corresponding attenuation structures (Fig. 9a) fit the observed waveform better. For W2 (Fig. 15b), although the VMOI-based model should fit even better as seen in Fig. 14a, the difference in waveforms seems subtle as the current modeling fits well.

During the review process of the current manuscript, the recent independent work of Attanayake et al. (2014) is called for the authors' attention by the referee and the editor. Our result is basically consistent with theirs except that our analyses cover a wider distant range, thus the models extend deeper in the inner core. The apparent inconsistency for some of the attenuation measurements might stem from the different ways of grouping of the measurements.

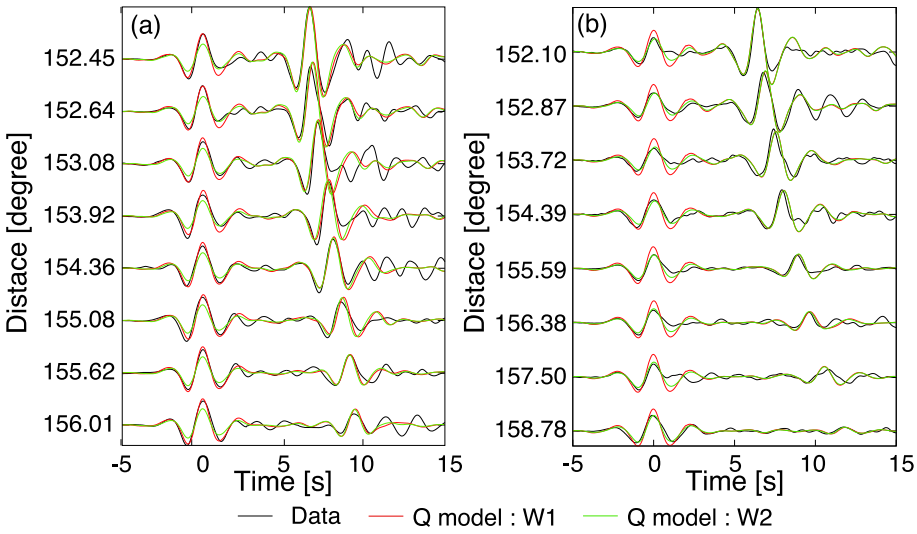

Fig. 15. Comparison of observed waveforms with synthetics for two attenuation models of the western hemisphere (Fig. 9a): (a) W1 (event: 26 July 2005 with PASSCAL array) and (b) W2 (4 March 2010 with NECESSArray). Red and green lines represent waveforms for the attenuation models of W1 and W2, respectively. DSM synthetics are convolved with the modeled reference waveform, $W(t)$. In each figure, waveforms are normalized by the amplitude of PKP(BC) at a smallest distant station (i.e., top traces in each figure). (For interpretation of the references to color in this figure legend, the reader is referred to the web version of this article.)

The well known positive correlation between velocity and attenuation in the inner core (e.g. Souriau et al., 2003) is confirmed in this study, and it is common to consider that seismic scattering is the primary mechanism for the attenuation in the inner core (e.g. Cormier and Li, 2002). Vidale and Earle (2000) suggested the existence of strong scattering due to heterogeneities with scale length of about 2 km in the top 300 km of the inner core by the envelope analysis of PKiKP coda. As a cause of scattering, the preferred alignment of iron crystals due to a dendritic growth of the iron is proposed to explain anisotropy of attenuation (Bergman, 1997; Bergman et al., 2002; Cormier and Li, 2002). While this interpretation of scattering well explains the anisotropic part of the attenuation and velocity, what we obtained in this study is a variation of the isotropic part (the equatorial paths) of attenuation and velocity. Therefore, it is necessary to consider a different texture to explain hemispherical heterogeneities of attenuation and velocity. Alternatively, Monnereau et al. (2010) and Alboussière et al. (2010) proposed a translational convection model of iron crystals of the inner core that crystallize in the western hemisphere side and melt (out to the outer core) in the eastern hemisphere side; this model explained the hemispherical variation of attenuation and velocity by the difference of the grain size (large grain size in the eastern hemisphere and small grain size in the western hemisphere). However, the translational convection does not result in any shear deformation. Therefore, the anisotropic feature that the polar rays go faster and are more attenuated than equatorial rays in the inner core (e.g. Poupinet et al., 1983; Creager, 1992; Shearer, 1994; Oreshin and Vinnik, 2004; Irving and Deuss, 2011) cannot be explained, as well as the heterogeneity of attenuation in the western hemisphere observed in this study. It may imply that more complex solidification process exists in the inner core. Iritani (2013) explored the possibility by extending the simulated annealing waveform inversion method to investigate the frequency dependency/independency of the inner core attenuation (*Iritani, Takeuchi, and Kawakatsu, paper in preparation*).

Acknowledgments

We thank all the members of the NECESSArray project, and staffs of IRIS, NIED, and ORFEUS data center for providing high-quality seismic data. We also thank S. Tanaka for helpful discussions and for the thorough review of the manuscript as a referee, and V. Cromier for helpful suggestions as the editor. The Generic Mapping Tools (Wessel and Smith, 1998) is used to draw some of the figures, and the Taup softwares (Crotwell et al., 1999) are used for the calculation of theoretical traveltimes. This work was supported by Grant-in-Aids for JSPS Fellows (23-10283) and by Grant-in-Aid for Scientific Research 19104011 provided by JSPS.

References

Aki, K., Richards, P.G., 1980. Quantitative Seismology. W.H. Freeman and Co., SanFrancisco, California.
Alboussière, T., Deduen, R., Melzani, M., 2010. Melting induced stratification above the Earth's inner core due to convective translation. Nature 466, 744–747.
Attanayake, J., Cormier, V.F., deSilva, S.M., 2014. Uppermost inner core seismic structure – new insights from body waveform inversion. Earth Planet. Sci. Lett. 385, 49–58.
Bergman, M.I., 1997. Measurements of elastic anisotropy due to solidification texturing and the implications for the Earth's inner core. Nature 389, 60–63.
Bergman, M.I., Cole, D., Jones, J., 2002. Preferred crystal orientations due to melt convection during directional solidification. J. Geophys. Res. 107, 2201.
Cao, A., Romanowicz, B., 2004. Hemispherical transition of seismic attenuation at the top of the Earth's inner core. Earth Planet. Sci. Lett. 228, 243–253.
Chevrot, S., 2002. Optimal waveform and delay time analysis by simulated annealing. Geophys. J. Int. 151, 164–171.
Cormier, V.F., 2009. A glassy lowermost outer core. Geophys. J. Int. 179, 374–380.
Cormier, V.F., Li, X., 2002. Frequency-dependent seismic attenuation in the inner core: 2. A scattering and fabric interpretation. J. Geophys. Res. 107, 2362.
Creager, K.C., 1992. Anisotropy of the inner core from differential travel times of the phases PKP and PKIKP. Nature 356, 309–314.
Creager, K.C., 1999. Large-scale variations in inner core anisotropy. J. Geophys. Res. 104, 23127–23139.
Crotwell, H.P., Owens, T.J., Ritsema, J., 1999. The TauP toolkit: flexible seismic travel-time and ray-path utilities. Seismol. Res. Lett. 70, 154–160. http://dx.doi.org/10.1785/gssrl.70.2.154.
Doornbos, D.J., 1974. The anelasticity of the inner core. Geophys. J. R. Astron. Soc. 38, 397–415.
Dziewonski, A., Anderson, D.L., 1981. Preliminary reference Earth model. Phys. Earth Planet. Inter. 25, 297–356.
Garcia, R., Chevrot, S., Weber, M., 2004. Nonlinear waveform and delay time analysis of triplicated core phases. J. Geophys. Res. 109, B01306.
Garcia, R., Tkalčić, H., Chevrot, S., 2006. A new global PKP data set to study the Earth's core and deep mantle. Phys. Earth Planet. Inter. 159, 15–31.
Iritani, R., 2013. Depth Variation of the Hemispheric Seismic Structure of the Inner Core Inferred from Global Seismic Array Data (Ph.D. thesis). Univ. of Tokyo. 113pp.
Iritani, R., Takeuchi, N., Kawakatsu, H., 2010. Seismic attenuation structure of the top half of the inner core beneath the northeastern Pacific. Geophys. Res. Lett. 37, L19303.
Irving, J., Deuss, A., 2011. Hemispherical structure in inner core velocity anisotropy. J. Geophys. Res. 116, B04307.

Kaneshima, S., Hirahara, K., Ohtaki, T., Yoshida, Y., 1994. Seismic structure near the inner core–outer core boundary. Geophys. Res. Lett. 21, 157–160.
Kawai, K., Takeuchi, N., Geller, R.J., 2006. Complete synthetic seismograms up to 2 Hz for transversely isotropic spherically symmetric media. Geophys. J. Int. 164, 411–424.
Kazama, T., Kawakatsu, H., Takeuchi, N., 2008. Depth-dependent attenuation structure of the inner core inferred from short-period Hi-net data. Phys. Earth Planet. Inter. 167, 155–160.
Kennett, B.L.N., Engdahl, E.R., Buland, R., 1995. Constraints on seismic velocities in the Earth from traveltimes. Geophys. J. Int. 122, 108–124.
Li, X., Cormier, V.F., 2002. Frequency-dependent seismic attenuation in the inner core: 1. A viscoelastic interpretation. J. Geophys. Res. 107, 2361.
Monnereau, M., Calvet, M., Margerin, L., Souriau, A., 2010. Lopsided growth of Earth's inner core. Science 328, 1014–1017.
Morita, Y., 1991. The attenuation structure in the inner-core inferred from seismic body waves. Central Core of the Earth 1, 65–75 (in Japanese).
Niu, F., Wen, L., 2001. Hemispherical variations in seismic velocity at the top of the Earth's inner core. Nature 410, 1081–1084.
Ohtaki, T., Kaneshima, S., Kanjo, K., 2012. Seismic structure near the inner core boundary in the south polar region. J. Geophys. Res. 117, B03312.
Oreshin, S., Vinnik, L., 2004. Heterogeneity and anisotropy of seismic attenuation in the inner core. Geophys. Res. Lett. 31, L02613.
Poupinet, G., Pillet, R., Souriau, A., 1983. Possible heterogeneity of the Earth's core deduced from PKIKP travel times. Nature 305, 204–206.
Sen, M., Stoffa, P., 1995. Global Optimization Methods in Geo-physical Inversion. Elsevier Sci, New York.
Shearer, P.M., 1994. Constraints on inner core anisotropy from PKP(DF) travel times. J. Geophys. Res. 99, 19647.
Souriau, A., Garcia, R., Poupinet, G., 2003. The seismological picture of the inner core: structure and rotation. C. R. Geosci. 335, 51–63.
Souriau, A., Roudil, P., 1995. Attenuation in the uppermost inner core from broadband GEOSCOPE PKP data. Geophys. J. Int. 123, 572–587.
Tanaka, S., 2012. Depth extent of hemispherical inner core from PKP(DF) and PKP(Cdiff) for equatorial paths. Phys. Earth Planet. Inter. 210–211, 50–62.
Tanaka, S., Hamaguchi, H., 1997. Degree one heterogeneity and hemispherical variation of anisotropy in the inner core from PKP(BC)–PKP(DF) times. J. Geophys. Res. 102, 2925–2938.
Vidale, J.E., Earle, P.S., 2000. Fine-scale heterogeneity in the Earth's inner core. Nature 404, 273–275.
Wessel, P., Smith, H.W.F., 1998. New, improved version of the Generic Mapping Tools released. Eos Trans. AGU 79, 579.
Yu, W., Wen, L., 2006. Seismic velocity and attenuation structures in the top 400 km of the earth's inner core along equatorial paths. J. Geophys. Res. 111, B07308.